

2018-12

# Residual crashworthiness of CFRP structures with pre-impact damage An experimental and numerical study

Chen, D

<http://hdl.handle.net/10026.1/12236>

---

10.1016/j.ijmecsci.2018.08.030

International Journal of Mechanical Sciences

Elsevier

---

*All content in PEARL is protected by copyright law. Author manuscripts are made available in accordance with publisher policies. Please cite only the published version using the details provided on the item record or document. In the absence of an open licence (e.g. Creative Commons), permissions for further reuse of content should be sought from the publisher or author.*

# **Residual crashworthiness of CFRP structures with pre-impact damage**

## **– An experimental and numerical study**

Dongdong Chen<sup>1</sup>, Guangyong Sun<sup>1,2,\*</sup>, Maozhou Meng<sup>3</sup>, Guangyao Li<sup>1</sup>, Qing Li<sup>2</sup>

<sup>1</sup>State Key Laboratory of Advanced Design and Manufacture for Vehicle Body,  
Hunan University, Changsha, 410082, China

<sup>2</sup>School of Aerospace, Mechanical and Mechatronic Engineering, The University of  
Sydney, Sydney, NSW 2006, Australia

<sup>3</sup>School of Marine Science and Engineering, Plymouth University, Plymouth, United  
Kingdom

### **Abstract**

This study investigated the effect of transverse pre-impact damage on the load bearing capacity and failure behavior of square carbon fiber reinforced plastic (CFRP) tubes for axial crushing. The CFRP tubes were impacted transversely in different levels of impact energies to generate initial damage, and then the specimens were further crushed axially to evaluate the relation between transverse impact energies/positions and the residual axial crashworthiness. A finite element (FE) model was also developed to simulate the complex damage behavior of the CFRP tubes under these two different loading processes, based upon the continuum damage model (CDM) with user-defined material subroutine in Abaqus. A combined failure mode was observed in the transverse pre-impact tests, in which delamination was combined with partial or complete fiber breakage when increasing the impact energy from 10 J to 30 J. In the axial compression tests, two typical failure modes with circumferential fracture near the pre-impact position were identified for the damaged tubes, exhibiting significant difference from the progressive folding failure seen in undamaged tubes. Further, the damaged tubes yielded up to 38%, 58.5% and 58.3% reduction in terms of the peak load, mean load and energy absorption respectively in comparison with the specimens without pre-impact damages. It is also found that the residual crushing capacity decreased with increase in the transverse pre-impact energy; nevertheless the residual axial crushing properties were insensitive to single or double impacts on different circumferential positions. The failure modes of fiber breakage, delamination and matrix crack were investigated in detail by using the FE analysis. **Keywords:** Residual crushing capacity; CFRP tube; Pre-impact damage; Crashworthiness

---

<sup>1\*</sup> Corresponding Author: Tel: +86-13786196408; Email: guangyong.sun@sydney.edu.au.

## 1. Introduction

Higher requirements of fuel efficiency and structural safety are in strong demand with intensifying socioeconomic legislation and industrial standard [1-3]. In general, these two aspects often conflict with each other [4]. One way to tackle this challenge is to replace traditional heavy metals with light-weight materials while remaining or even enhancing the structural performances. In this regard, carbon fiber reinforced plastic (CFRP) composites have been exhibiting significant potential thanks to their extraordinary capacity of weight to specific stiffness, strength and energy absorption [5].

To understand crash behavior of CFRP structures, substantial experimental studies have been conducted on crashworthiness of various tubal components. For example, Mamalis et al. [6, 7] investigated the different collapse modes of square CFRP composite tubes subjected to static and dynamic axial crashes, and they found that only the progressive crushing mode absorbed the highest energy. They also identified that the peak crushing load increased with increase of wall thickness and fiber volume content. Jia et al. [8] investigated the quasi-static crushing behavior of filament wound CFRP cylinder with different geometric parameters, winding angles and pre-crack angles. They concluded that the evolution process of failure mostly depended on the pre-crack angle which would cause the crack initiation. Siromani et al. [9] studied three typical failure trigger modes to identify their effects on initial peak load and specific energy absorption (SEA); and they showed that combing a chamfered tube with an inward-folding crush-cap yielded the lowest initial peak load and the highest SEA. Liu et al. [5] analyzed the effects of wall thickness and lengths of the double hat shaped CFRP tubes; they identified two distinctive failure modes through the dynamic tests, which differed with a typical mode of continuous splaying fronds in quasi-static tests. They also reported that increasing impact velocity would increase the peak load but decrease the energy absorption (EA) and specific energy absorption (SEA). Meredith et al. [10] explored the effects of manufacture processes (e.g. vacuum assisted oven cure and autoclave cure) on crash performance of CFRP cones through dynamic impact tests, in which performance versus cost analysis was conducted, revealing enormous potential for cost reduction of prepreg carbon fiber epoxy cones through use of heavier areal weight fabrics with fewer plies as well as through use of oven cured prepreg.

Numerical modeling represented by finite element method has gained growing popularity for its advantages in simulating mechanical behaviors of composite tubes in detail.

For example, McGregor et al [11] adopted the continuum damage mechanics model (CDM) to predict axial impact of two-ply and four-ply square tubes with and without an external plug initiator using LS-DYNA; and good agreement was obtained in terms of the failure characteristics and energy absorption. Zhu et al. [12] proposed two different numerical models, namely multi-layer stacked model and single-layer shell model, to simulate the crushing process of CFRP structures; and they found that the multi-layer stacking model exhibited a better capability of predicting the main failure modes and crashworthiness of the CFRP structures. Obradovic et al. [3] carried out the experimental, analytical and numerical studies on the crash analysis of composite structures under frontal impact, demonstrating the critical importance of selecting failure criteria for predicting brittle collapse. In literature, some typical composite damage models, e.g. MAT58 and MAT54 in LS-DYNA, were validated and have proven to be effective for simulating the inter-ply delamination under axial crushing [13, 14]. Two different finite element (FE) models, namely stacked shell model and crushing zone model, were developed for predicting the energy absorption in the crushing process [15]. However, these abovementioned FE models have not model complex failure mechanism of CFRP tubes for predicting crushing process and energy absorption.

It is well known that CFRP composite structures are very sensitive to dynamic loading; and even a minor, invisible damage could cause noticeable reduction in the strength and stiffness [16]. Therefore, it is crucial to evaluate the load-bearing capacity of composite structures with any pre-existed damage at different levels. In literature, there have been some studies available on evaluating the residual performance of CFRP structures with some pre-generated holes, defects and/or damages. In this regard, Liu et al. [17] undertook an experimental and numerical study on the load bearing behavior of square CFRP tubes with open holes subjected to axial compression; the effects of hole sizes, shape and distribution on the first peak force, failure modes and SEA were explored. It exhibited that the hole size had the stronger effect on peak load and SEA than hole shape and distribution. Guades and Aravinthan [18] conducted an experimental study on the residual properties of square pultruded tubes made of E-glass fiber composites subjected to axial impact, in which the coupons taken around the impacted area were tested with compressive, tensile and flexural loadings. Their study revealed that the residual strength of the pre-impacted tubes degraded with the pre-impact energy, number of impacts and mass of the impactor, whilst little effect appeared on the residual modulus. Sebaey and Mahdi [19] studied the quasi-static transverse crushing characteristics of glass/epoxy pipes by introducing impact damage. They found that the peak load was reduced by 23% for top/bottom pre-impacted tube and 15% for the side

pre-impacted tube in comparison with those of the non-impacted ones, meaning that the capacity of resisting crash was reduced due to the pre-impacted damage. With the increase in the impact energy and impact numbers, such a reduction trend could be also seen in the peak force and average crushing load.

In literature, most of the existing numerical studies on residual mechanical response of composites have been focused on laminates [20-25]. For example, Wang et al. [20] developed a FE model to simulate the low-velocity impact characteristics and predicted the residual tensile strength, in which a progressive damage model with stress-based Hashin criteria was used to model the fiber and matrix failures of the CFRP laminates under impact load. Abir et al. [21] investigated the effects of impact damage on crushing performance of CFRP laminates numerically, in which the continuum damage mechanics (CDM) model and cohesive interface elements were adopted to characterize the fiber failure and inter-laminar fracture behavior. Tan et al. [22] adopted a three-dimensional composite damage model to simulate the fiber failure and delamination behavior under the so-called compression-after-impact (CAI) test; and good agreement was obtained between the numerical and experimental results in terms of force-displacement curves, damage contours and permanent indentation. As for the composite laminates reinforced by unidirectional fibers, the cohesive connections were introduced only in the areas between the plies with different fiber orientations for reducing the computational cost [23]; and the simulated results showed fairly good accuracy on modeling the complex failure phenomena during crushing after the initial impact tests.

The previous study indicated that the CFRP tubes are of sizeable advantages on crashworthiness than aluminum counterparts under quasi-static axial loading [26]. There is a great potential of replacing traditional metallic energy absorbers with CFRP structures attributable to its high energy absorption and lightweight performance. Crash box, as one important application for energy absorption, could be subjected to various impact loading during its life cycle, such as tools dropping (assembling process) or collision from ground pebbles (travel process), representing accumulative damage from different pre-impacts. Unfortunately, only few studies have been available in literature for evaluating the residual crushing behavior of composite tubes with pre-introduced damage. In this regard, Liu et al. [17] investigated the damage mechanisms of perforated CFRP tubes under quasi-static crushing. Their FE model was able to model the crack initiation, propagation and strain distribution around the pre-perforated hole edges accurately. Deniz et al. [27] explored the low-velocity crushing with pre-impacted damage in the  $[\pm 55]_3$  filament-wound glass/epoxy composite circular tubes. To the author's best knowledge, nevertheless, there has been no

study available to explore the complex damage mechanism for the axial crash with pre-impacted damage laterally. It remains to identify the residual axial crashworthiness for the CFRP tubes with pre-impacted damage in the transverse direction.

This study aimed to provide an experimental and numerical investigation into the residual load bearing capacity of the CFRP tubes with lateral pre-impacted damage. The failure modes and force-displacement curves characterized by different impact energies were analyzed, and then the damage mechanisms induced by different loading levels were discussed based upon the optical observations on the fractured area. The effects of impact parameters such as impact energy and impact position on the residual axial crushing properties were investigated in detail. The study is expected to provide a guideline for quantifying residual crashworthiness of CFRP tubes with pre-damage in a different direction.

## **2. Materials and experimental methods**

### **2.1. Materials**

Square CFRP tubes were fabricated from plain weave fabric carbon-epoxy pre-preg (provided by Toray industries [12]) by using the bladder molding process. The tube walls were constructed with 9 layers, having 1.98mm in thickness, 100mm in length and 60mm in side width. The stacking sequence of piles was in a form of  $[0^\circ/90^\circ]$ . All the specimens were prepared with the  $45^\circ$  chamfer of 1mm, as shown in Fig. 1(c).

### **2.2. Low-velocity pre-impact tests**

The low-velocity pre-impact tests were performed using INSTRON 9350 drop weight testing machine. A hemispherical impactor with 20 mm in diameter and  $m = 2.41$  kg in mass was chosen for the tests. Different incident impact energies can be generated by changing the initial height of the impactor. A pressure of 500 N was applied on the fixtures to clamp the CFRP tube during the impact test as shown in Fig. 1. Two support blocks (fit to the inner dimension of the tube as  $56 \cdot 56 \cdot 20$  mm) were manufactured and placed in each end of the CFRP tube to replicate the real assembly condition and avoid excessive deformation during the crash tests.

Two pre-impact parameters, namely the impact position and impact energy, were considered in this study. For each energy level, three repeats were performed and the results were summarized in Table 1. A labelling system was used to facilitate the analysis and comparison. For example, AC indicates that tubes were crashed axially without any pre-impacted damage, which serves as the comparison (control) group. The effects of pre-impact

were investigated as per E1-P1, E2-P1 and E3-P1, meaning that the tubes were impacted at the same impact position (P1 as shown in Fig. 2) but different pre-impact energies (E1/E2/E3, representing 10/20/30 J to generate different levels of damage during the transverse pre-impaction). The number of impacts and impact energy for E2-P2 and E2-P3 were the same, i.e. 2 times, and each with the same level of 20 J separately; but at the different impact locations, i.e. P2 and P3 as shown in Fig. 2. The impact position on the impacted face was the same for every impact test, i.e. the same coordinate as the P1 cases but on the different faces.

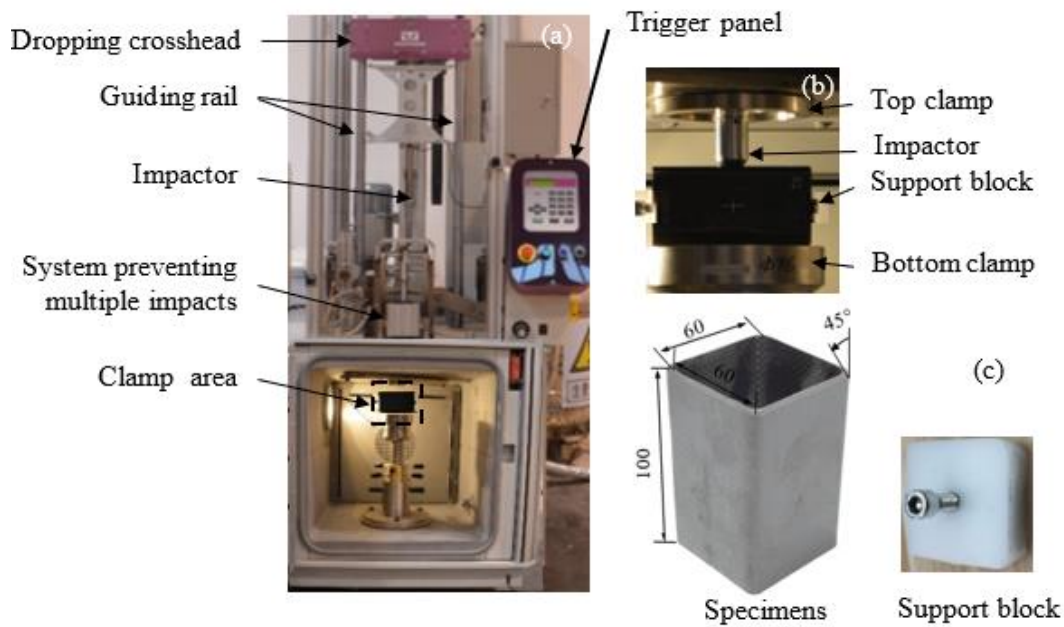


**Fig. 1.** Illustration of the low-velocity impact test system: (a) low-velocity test set-up, (b) enlarged view of the clamp area, and (c) details for specimen and support blocks (unit: mm).

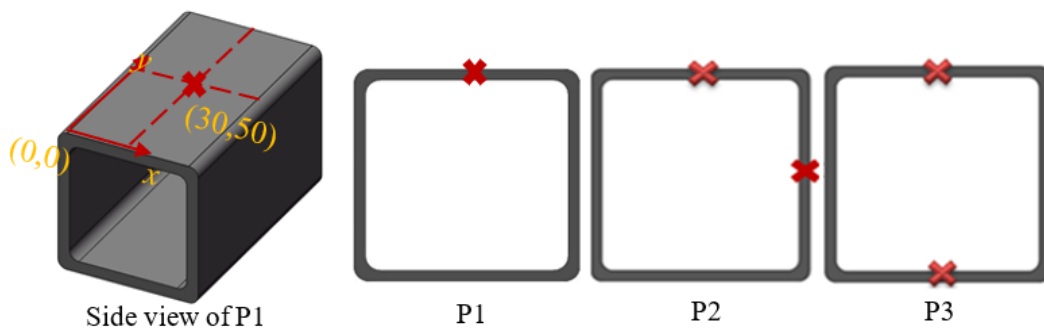


**Fig. 2.** Positions of the impacts in three cases (unit: mm, red X represents the impact point).

**Table 1**  
Crashworthiness characteristics of the tested specimens.

| Tube label | Impact    |           |                | After impact |                |                 |            |      |
|------------|-----------|-----------|----------------|--------------|----------------|-----------------|------------|------|
|            | $E_i$ (J) | $E_a$ (J) | $P_{max}$ (kN) | Failure mode | $P_{max}$ (kN) | $P_{mean}$ (kN) | $E_a$ (kJ) | CFE  |
| AC-1       | 0.0       | 0.0       | 0.0            | I            | 77.8           | 60.3            | 48.3       | 0.78 |
| AC-2       | 0.0       | 0.0       | 0.0            | I            | 86.9           | 58.8            | 47.1       | 0.68 |
| AC-3       | 0.0       | 0.0       | 0.0            | I            | 85.1           | 61.7            | 49.4       | 0.72 |
| Average    | 0.0       | 0.0       | 0.0            |              | 83.2           | 60.3            | 48.3       | 0.72 |

|         |      |      |     |     |      |      |      |      |
|---------|------|------|-----|-----|------|------|------|------|
| S.D.    | 0.0  | 0.0  | 0.0 |     | 3.9  | 1.2  | 0.9  | 0.04 |
| E1-P1-1 | 10.0 | 7.6  | 2.2 | II  | 68.7 | 43.1 | 34.5 | 0.63 |
| E1-P1-2 | 10.0 | 7.2  | 2.1 | II  | 69.5 | 30.7 | 24.6 | 0.44 |
| E1-P1-3 | 10.0 | 7.4  | 2.5 | I   | 65.1 | 51.5 | 41.2 | 0.79 |
| Average | 10.0 | 7.4  | 2.3 |     | 67.8 | 41.8 | 33.4 | 0.62 |
| S.D.    | 0.0  | 0.2  | 0.2 |     | 1.9  | 8.5  | 6.8  | 0.14 |
| E2-P1-1 | 20.0 | 18.7 | 2.3 | III | 60.4 | 28.7 | 23.0 | 0.48 |
| E2-P1-2 | 20.0 | 18.6 | 2.2 | III | 56.1 | 20.6 | 16.5 | 0.38 |
| E2-P1-3 | 20.0 | 17.6 | 2.0 | III | 60.7 | 24.8 | 19.9 | 0.41 |
| Average | 20.0 | 18.3 | 2.1 |     | 59.0 | 24.7 | 19.8 | 0.42 |
| S.D.    | 0.0  | 0.5  | 0.1 |     | 2.1  | 3.3  | 2.7  | 0.04 |
| E3-P1-1 | 30.0 | 19.5 | 2.3 | III | 54.6 | 34.3 | 27.5 | 0.63 |
| E3-P1-2 | 30.0 | 20.4 | 2.2 | III | 61.9 | 33.6 | 26.9 | 0.54 |
| E3-P1-3 | 30.0 | 21.5 | 2.3 | III | 63.0 | 33.1 | 26.5 | 0.53 |
| Average | 30.0 | 20.5 | 2.3 |     | 59.8 | 33.7 | 27.0 | 0.56 |
| S.D.    | 0.0  | 0.8  | 0.0 |     | 3.7  | 0.5  | 0.4  | 0.04 |
| E2-P2-1 | 20.0 | 18.3 | 2.2 | III | 62.8 | 25.0 | 20.0 | 0.4  |
| E2-P3-1 | 20.0 | 18.8 | 2.2 | III | 51.5 | 28.7 | 23.0 | 0.56 |

S.D. means the standard deviation.

### 2.3. Axial crush after transverse pre-impacts

Quasi-static axial crushing tests for the pre-impacted specimens were carried out in a standard universal testing machine INSTRON 5985 with a load capacity of 150 kN. A constant cross-head velocity of 4 mm/min was set throughout the test at the room temperature. All the specimens were crushed up to 80% of their original length, i.e. 80mm. The detailed deformation and failure process were recorded by a camera with the displacement interval of 2 mm. For comparison, the tests with non-pre-impacted specimens were also conducted.

A crashworthy structure should have excellent capacity of absorbing sufficient energy with a low peak crushing force. In literature, four different indicators were often adopted to evaluate the crashworthiness of structures [28]. The peak force ( $P_{max}$ ), which is the maximum force value in the displacement-force curves recorded from the tests, should be as low as possible to protect the occupants from fatal injuries [28]. The mean crushing force ( $P_{mean}$ ) was used to measure the energy absorption as:

$$P_{mean} = \frac{1}{L} \int_0^L PdU \quad (1)$$

where  $P$  and  $U$  are the crush load and displacement, respectively;  $L$  is the total displacement.

The crush force efficiency ( $CFE$ ) can be used to evaluate the variation of  $P_{mean}$  relative to  $P_{max}$ , which should be close to 1 for the best possible force level,

$$CFE = \frac{P_{mean}}{P_{max}} \quad (2)$$

The energy absorption ( $E_a$ ) is the energy dissipated during the crushing process as calculated mathematically by:

$$E_a = \int_0^L PdU \quad (3)$$

### 3. Two-stage finite element modeling

#### 3.1. Failure model

Finite element method was adopted to investigate the damage accumulation and evolution in the CFRP tube during the transverse pre-impact and subsequent axial crushing process. Axial crushing behaviors of CRFP composite post low velocity pre-impact are of significant implication since it could reduce the structural performance without giving any visible signs. Damage induced by low velocity pre-impact can be analyzed in terms of various numerical models [29], in which a CDM model was adopted to predict the complex failure modes of CFRP laminate [22, 30]. The computational work was performed in ABAQUS 6.13/Explicit in this study.

##### 3.1.1. Fiber failure modeling

Complex failure modes exist for the CFRP tubes subjected to axial crushing after the transverse pre-impact loading, which includes fiber breakage, pull-out, matrix crack and delamination of adjacent plies [21]. The CDM stress-strain model as presented in [12, 30], was adopted and modified here as follows.

The woven fabric reinforcement considered here was configured in the orthogonal directions. The stiffness degradation between the stress and strain ( $\sigma_{ij}$  and  $\varepsilon_{ij}$ ) can be expressed as [30]:

$$\begin{Bmatrix} \varepsilon_{11} & \varepsilon_{22} & \varepsilon_{12}^{el} \end{Bmatrix} = \begin{bmatrix} \frac{1}{(1-d_1)E_1} & \frac{-\nu_{12}}{E_1} & 0 \\ 0 & \frac{-\nu_{21}}{E_2} & \frac{1}{(1-d_2)E_2} \\ \frac{1}{(1-d_{12})2G_{12}} & 0 & 0 \end{bmatrix} \begin{Bmatrix} \sigma_{11} & \sigma_{22} & \sigma_{12} \end{Bmatrix} \quad (4)$$

where subscripts 1 and 2 represent the longitudinal and transverse fiber directions, respectively;  $\varepsilon_{12}^{el}$  represents the elastic strain in the shear direction.  $E_1$ ,  $E_2$  and  $G_{12}$  are initial in-plane stiffnesses in the longitudinal, transverse and shear directions;  $\nu_{12}$  and  $\nu_{21}$  are in-plane Poisson's ratios;  $d_1$  and  $d_2$  are damage variables accounting for the effect of fibers on mechanical responses once fiber damage is initiated;  $d_{12}$  is matrix failure parameter under shear loading.

Once the initial damage appears in the composite, evolution of the fiber damage variables  $d_1$ ,  $d_2$  and  $d_{12}$  are calculated as [30]:

$$d_1 = d_{1+} \frac{\langle \sigma_{11} \rangle}{|\sigma_{11}|} + d_{1-} \frac{\langle -\sigma_{11} \rangle}{|\sigma_{11}|} \quad (5)$$

$$d_2 = d_{2+} \frac{\langle \sigma_{22} \rangle}{|\sigma_{22}|} + d_{2-} \frac{\langle -\sigma_{22} \rangle}{|\sigma_{22}|} \quad (6)$$

$$d_\alpha = 1 - \frac{1}{r_\alpha} \exp\left[-\frac{2g_0^\alpha L_c}{G_f^\alpha - g_0^\alpha L_c} (r_\alpha - 1)\right] \quad (7)$$

$$d_{12} = \min[\beta_{12} \ln \ln(r_{12}), d_{12}^{max}] \quad (8)$$

where  $\alpha = 1 \pm, 2 \pm$ , so that  $d_{1+}$ ,  $d_{2+}$  and  $d_{1-}$ ,  $d_{2-}$  denote the tensile and compressive damage states, respectively;  $\langle x \rangle$  is the Macaulay operator which is defined as  $\langle x \rangle = (x + |x|)/2$ ;  $r_\alpha$  is the damage threshold for fiber which is defined in terms of  $F_\alpha$  (failure coefficients corresponding to tensile or compressive failure) in Eqs. (9)-(10) below;  $g_0^\alpha$  denotes the elastic energy per unit volume under uniaxial tensile or compressive loading;  $G_f^\alpha$  is the fracture energy per unit area for fiber tensile or compressive failure;  $L_c$  denotes the characteristic length of the element;  $\beta_{12}$ ,  $r_{12}$  and  $d_{12}^{max}$  represent the material parameters needed for the matrix and  $r_{12}$  is defined in terms of  $F_{12}$  (failure coefficient for matrix damage) in Eq. (11) below.

$$r_{i+} = \max(1, F_{i+}) \quad (9)$$

$$r_{i-} = \max(1, F_{i-}) \quad (10)$$

$$r_{12} = \max(1, F_{12}) \quad (11)$$

The damage thresholds are initially set to be 1 prior to composite failure and updated in each iterative analysis step in the damage evolution process. This means that the damage threshold varies and damage history of composite needs to be updated accordingly.

The critical issue is how to decide the initiation of various modes of damage. In this study, the effective stress  $\hat{\sigma}_{i+}$  ( $i = 1, 2$ ) [30] is adopted as Eqs. (12)-(14). The failure criteria for fiber tensile/compressive breakage and matrix crack are then defined in Eqs. (15)-(17).

$$\hat{\sigma}_{i+} = \frac{\langle \sigma_{ii} \rangle}{1 - d_{i+}} \quad (12)$$

$$\hat{\sigma}_{i-} = \frac{\langle -\sigma_{ii} \rangle}{1 - d_{i-}} \quad (13)$$

$$\hat{\sigma}_{12} = \frac{\sigma_{12}}{1 - d_{12}} \quad (14)$$

$$F_{i+} = \frac{\hat{\sigma}_{i+}}{X_{i+}} \quad (15)$$

$$F_{i-} = -\frac{\hat{\sigma}_{i-}}{X_{i-}} \quad (16)$$

$$F_{12} = \left| \frac{\hat{\sigma}_{12}}{S} \right| \quad (17)$$

where  $X_{i+}$  and  $X_{i-}$  are the tensile and compressive strengths in the longitudinal and transversal directions, namely  $i = 1$  and  $i = 2$ , respectively;  $S$  is the in-plane shear strength. The corresponding failure behavior should be considered if one of the failure criteria has

reached (the corresponding failure coefficient  $F$  is equal to 1.0).

In literature, it was found that the fiber failure dominates the failure mode during the pre-impact stage [20, 21, 24]. In this situation, mechanical behavior of matrix was linear elastic, in which the stress components degraded to 0 directly after tensile/compressive strengths had been reached/violated. Note that it is unnecessary to consider the complex plastic behavior of the matrix, but the damage of CFRP plies should be considered because it could significantly change load transfer under axial crushing test.

The modeling strategy for the square CFRP tubes subjected to quasi-static axial crushing was established in [12] through the experimental validation. The computational parameters used for numerical modeling were obtained from our previous study [12]. The compressive fracture energy were obtained from [31] and tensile fracture energy was adopted to be half of compressive values as suggested in [12, 30]. The material properties of the CFRP used for finite element modeling are summarized in Table 2.

**Table 2**  
Material parameters used for the finite element analyses.

| Property  | value |
|---|-------|
| Density, $\rho$ (kg/m <sup>3</sup> )                          | 1560  |
| Longitudinal modulus, $E_1$ (GPa)                             | 65.1  |
| Transversal modulus, $E_2$ (GPa)                              | 64.4  |
| Poisson's ratio, $\nu_{12}$                                   | 0.037 |
| Shear modulus, $G_{12}$ (GPa)                                 | 4.5   |
| Longitudinal tensile strength, $X_{1+}$ (MPa)                 | 776   |
| Longitudinal compressive strength, $X_{1-}$ (MPa)             | 704   |
| Transversal tensile strength, $X_{2+}$ (MPa)                  | 760   |
| Transversal compressive strength, $X_{2-}$ (MPa)              | 698   |
| Shear strength, $S$ (MPa)                                     | 95    |
| Longitudinal tensile fracture energy (kJ/m <sup>2</sup> )     | 40    |
| Longitudinal compressive fracture energy (kJ/m <sup>2</sup> ) | 82    |
| Transversal tensile fracture energy (kJ/m <sup>2</sup> )      | 38    |
| Transversal compressive fracture energy (kJ/m <sup>2</sup> )  | 80    |

### 3.1.2. Delamination modeling

The inter-laminar failure mechanism was modeled by using the cohesive contact technique as suggested in [12, 22]. Before delamination appeared, linear elastic behavior is considered in the normal and shear directions, respectively. The initiation of damage is based on the quadratic traction-separation criteria as [32]:

$$\left(\frac{\langle t_n \rangle}{t_n^0}\right)^2 + \left(\frac{\langle t_s \rangle}{t_s^0}\right)^2 + \left(\frac{\langle t_t \rangle}{t_t^0}\right)^2 = 1 \quad (18)$$

where  $t_n$ ,  $t_s$ ,  $t_t$  and  $t_n^0$ ,  $t_s^0$ ,  $t_t^0$  are the traction and interface strength in the normal and shear

directions, respectively.

Once the failure criteria are satisfied, the delamination between CFRP plies propagates according to the mixed-mode damage evolution law as:

$$G_n^C + (G_S^C - G_n^C) \left( \frac{G_S + G_t}{G_n + G_S} \right)^\eta = 1 \quad (19)$$

where  $G_n^C$ ,  $G_S^C$  and  $\eta$  are the critical fracture toughness parameters;  $G_n$ ,  $G_S$  and  $G_t$  represent the work done by the traction in the normal and shear directions, respectively. Table 3 lists the inter-laminar damage parameters used in this study.

**Table 3**  
Inter-laminar properties for CFRP tube [12].

| Property                                      | value |
|---|-------|
| Damage initiation $t_n^0$ (MPa)               | 54    |
| Damage initiation $t_s^0$ (MPa)               | 70    |
| Damage initiation $t_n^0$ (MPa)               | 70    |
| Fracture energies $G_n^C$ (J/m <sup>2</sup> ) | 504   |
| Fracture energies $G_S^C$ (J/m <sup>2</sup> ) | 1566  |
| Fracture energies $G_t^C$ (J/m <sup>2</sup> ) | 1566  |
| $\eta$  | 2.284 |

### 3.2. CAI model

In this study, the FE model was developed in ABAQUS 6.13/Explicit to simulate the complex deformation and failure process during the CAI test. The schematic is shown in Fig. 3. The constitutive law for CFRP tube was coded based upon the constitutive laws as defined in Section 3.1.1 with a VUMAT subroutine in ABAQUS.

The impactor was modeled as a rigid body with mass of 2.3 kg. The fixtures were all modeled as rigid body. The square CFRP tube wall was meshed with 9 plies (the same number of plain weave fabric layers adopted for the experimental specimens) using the 3D continuum shell elements (SC8R) in ABAQUS. According to the mesh refinement study in [21], a mesh size of 1.0 ·1.0 mm was adopted for the CFRP plies to predict the mechanical responses with a proper balance of computational accuracy and efficiency. It should be noted that to reduce the computational cost, several modeling techniques were also used here: only one element across the thickness direction of each ply was meshed similarly to that in [23]; the inter-laminar interaction between the plies was modeled with cohesive behavior as defined in section 3.1.2. Table 4 shows more details of the mesh definition.

The general contact algorithm was adopted here to simulate possible contact interaction between the impactor, platens, fixtures and the CFRP tube walls in the FE simulation. A

tangential friction coefficient was set to be 0.15 since changing friction coefficient had rather limited effect on the main collapse modes and crushing characteristics [12].

The FE analysis was conducted in four steps to simulate the real experimental conditions (Fig. 3): (1) The pre-impact loading was applied by the impactor with specified energy level while the other parts remained unchanged; (2) The impactor, top/bottom fixtures and two blocks were removed while both the platens (front and back platen) moved away from their initial positions toward the tube quickly with a little clearance; (3) Both the platen moved slowly toward the pre-impacted tube to minimize the effect on equilibrium state of the CFRP tube; (4) The front platen moved longitudinally to simulate the axial crushing process after steps (2) and (3). Although the experimental crushing tests were carried out quasi-statically (4 mm/min), an average loading rate of 1 m/s was applied numerically and mass scaling technique for composite tube was adopted in the crushing process in ABAQUS/Explicit solver to reduce the computational cost while maintain the numerical accuracy as suggested in [30].

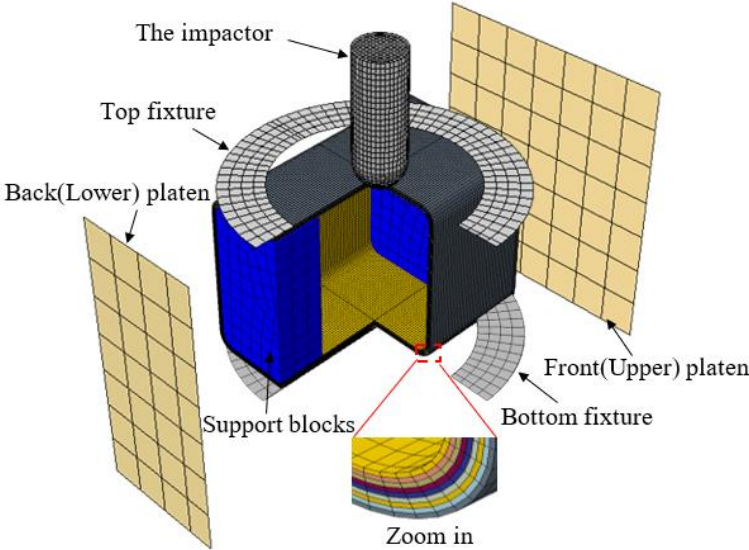


Fig. 3. CAI set-up model.

**Table 4**  
Mesh details in the finite element models.

| Model     | Element type | Element number |
|-----------|--------------|----------------|
| Impactor  | C3D8R        | 4,440          |
| Fixtures  | R3D4         | 576            |
| Platens   | R3D4         | 98             |
| Blocks    | C3D8R        | 666            |
| CFRP tube | SC8R         | 196,080        |
| Total     | -            | 201,860        |

## 4. Results and Discussion

### 4.1. Pre-impact tests

Three pre-impact energies were adopted to investigate the effect of impact energy on the CFRP tubes in this study. Typical force-displacement curves were used to evaluate the pre-impact characteristics. Deformation patterns around the pre-impact position were used to identify the failure mechanism. Finally, the effects of impact energy on transverse pre-impact mechanical characteristics were quantified.

#### 4.1.1. Pre-impact force-displacement relationship

The dynamic contact force-displacement curves during the pre-impact process were plotted in Fig. 4, in which the test results listed here all had the same impact number of one and impact position. A hill-like shape with an ascending and descending range for loading variation appeared for all the curves during the pre-impact process. Two typical patterns were observed due to the difference in the descending stage, namely partial unloading and fully perforating similarly to [33]. Some common features could be observed that the contact force between the impactor and specimen increased with the impactor movement prior to the peak force.

Correspondingly, several failure modes were unveiled in the impact/penetration area during the pre-impact process as: matrix crack, fiber breakage and delamination between adjacent plies [33]. In the case of pre-impact with 10 J energy (E1-P1), the deflection decreased after the peak point but did not return to the origin point as the load decreased to zero. This is classified as a partial rebounding process, which means that a permanent indentation had been caused, generating a local damage and reducing the structural stiffness/strength.

For the impact energy of 20 J and 30 J with the same impact number and position (E2-P1 and E3-P1), a plateau can be seen on the top zone of the curves, which indicates that the peak force did not drop immediately, instead maintained at a higher level for a while prior to perforation. Finally, the contact force decreased to zero with the increase of impactor displacement, indicating a complete perforation of the pre-impacted side surface on the CFRP tube. Note that no rebound was observed for these two impact energies.

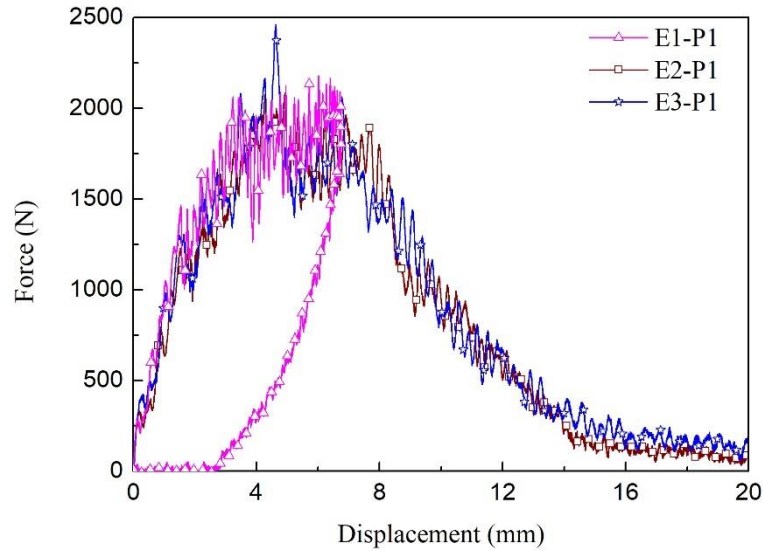


**Fig. 4.** Typical force-displacement curves under impact with different levels of impact energies.

#### 4.1.2. Failure mechanisms and energy absorption

As displayed in Fig. 5, the CFRP tubes showed different damage modes, depending on the pre-impact energies. The common cross-shaped cracks were generated on the pre-impacted face, which were associated with matrix crack and delamination. As illustrated in Fig. 5, the composite laminate was perforated with a circular shape of damage zone under impact energy of 30 J, in which the diameter of the damage zone was the biggest and even larger than that of the impactor, indicating a full perforation damage. Interestingly, the area of damage zone increased with decrease of impact energy from 30 J to 10 J, while failure mode varies from entire fiber breakage to matrix cracking and delamination.

Cross-sectional view of the impacted area which was obtained by using a Leica DVM6 optical microscopy is shown in Fig. 6. The primary damage modes were matrix crack and delamination, which grew through-the-thickness at the pre-impacted area. A slight fiber breakage can be also seen on the bottom face due to the tension induced by the tendency of pre-impact penetration. With the increase of impact energy to 20 J, the carbon fibers at the impact area failed completely, broke into four pieces as shown in Fig. 5. For the case of impact energy 30 J, all the damage modes appeared in the lower energy impact can be found here, implying that there was no other damage mode appeared in this case.

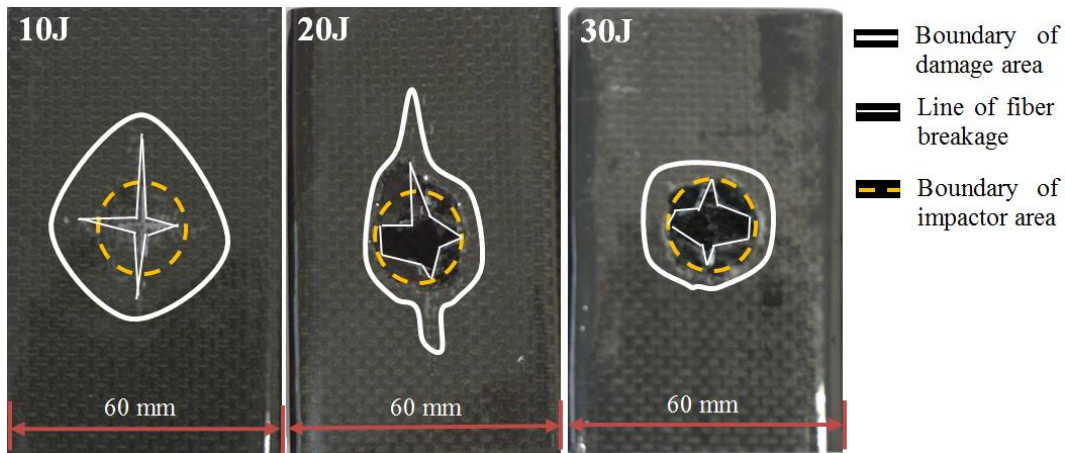


**Fig. 5.** Damage modes of composite tubes after impact with various energies.

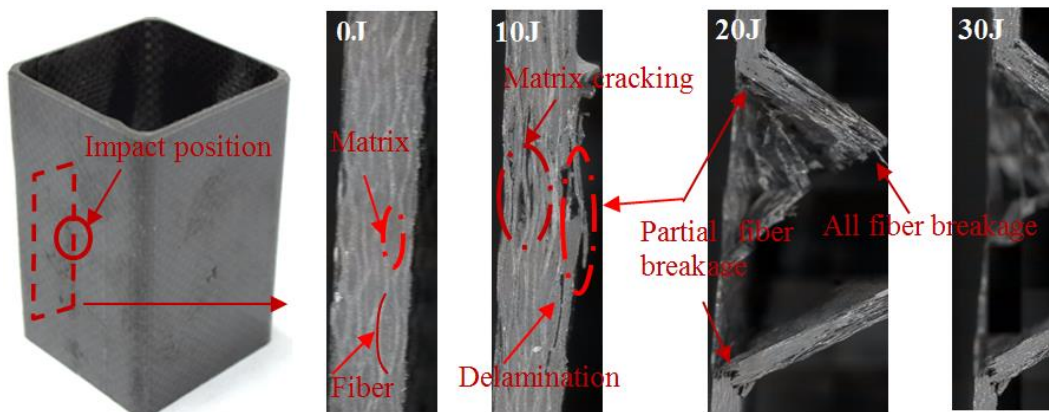


**Fig. 6.** Cross-sectional views of the impacted area.

#### 4.1.3. Effects of impact energy on pre-impact behavior

Energy absorption is the energy absorbed by the specimens during loading process which could be calculated from the area of load-displacement curve. Table 1 summarized the results obtained from the force-displacement curves. In this case, the crashworthiness criteria  $E_a$  (energy absorption) and  $P_{max}$  (maximum crushing force) were used to evaluate the residual performance of the specimen under pre-impact loading.

From Fig. 7(a), it is interesting to note that the maximum impact forces kept almost as a constant with increase of the impact energy. This phenomenon agrees well with that of CFRP laminates impacted with different levels of energies as reported in [16], where a relatively small fluctuation of maximum force could be found around the penetration energy. On the other hand, Fig. 7(b) shows that the average residual energy absorption of the CFRP specimens increased dramatically from 7.4 J to 18.3 J with the increase of the pre-impact energy from 10 J to 20 J; but a lower increase value of 2.2 J appears when the pre-impact energy increased from 20 J to 30 J. This can be explained according to the damage modes as shown in Fig. 6. Impact energy is mostly absorbed as matrix cracking, delamination and fiber

breakage in the pre-impact process, meaning no noticeable increase in fiber breakage or matrix failure area when increasing the impact energy from E2 (20 J) to E3 (30 J).

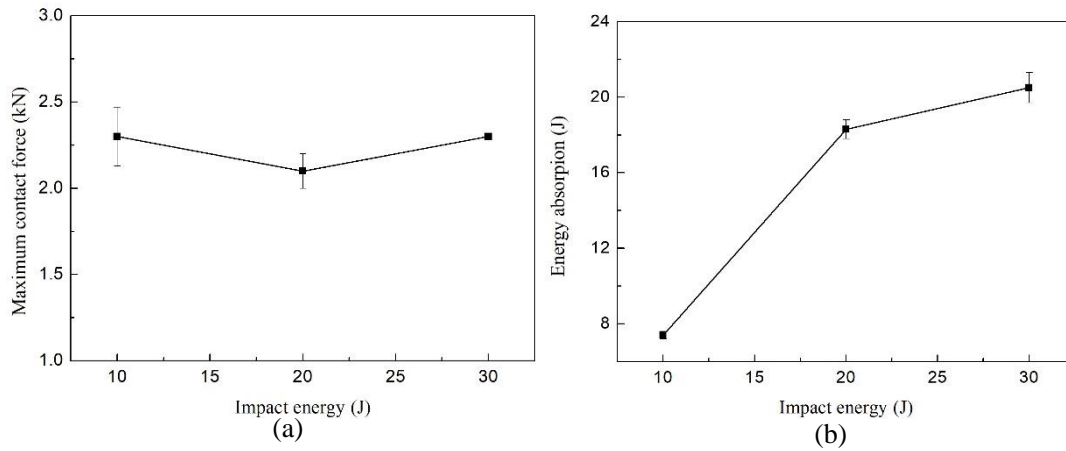


**Fig. 7.** Effects of pre-impact energy on: (a) maximum pre-impact force, (b) energy absorption.

## 4.2. Axial crushing tests

In this section, the further axial crushing process is investigated, in which the crushing force-displacement curves and damage mechanics were analyzed for the CFRP tubes with transverse pre-impact damage. Specifically, the effects of the pre-impact induced damage on the axial crashworthiness are studied quantitatively here. For comparison, the CFRP tubes with pre-impact energy of 0 J (non-impacted) was also analyzed in section 4.2.1.

### 4.2.1. Non-impacted specimens

A typical crushing force-displacement curve for the non-impacted specimen is plotted in Fig. 8(a), showing its progressive failure behaviors in three different loading stages. The axial crushing load increased rapidly to a peak (approximately 80 kN at the displacement of 1.9 mm) after the loading platen contacted on the end of the non-impacted CFRP tube, which was named as pre-crushing stage as in [12]. Then the load dropped slightly to a plateau level with small fluctuations, which was known as the post-crushing stage, where the cracks between the CFRP plies propagated progressively along the axial direction, leading to a steady failure state (defined as failure mode I in Table 1). The mean load was extracted to characterize the overall resistance to the quasi-static axial crushing in this stage.

In this non-impact case, the composite tube was split into four unbroken pieces due to stress concentration at the four corners. The cracks initiated from the incident end and then split the walls into inward and outward fronds as seen in Fig. 8(b)-(c). It is seen that a wedge

was formed at the interface of the inward and outward fronds, which separated the wall into two halves continuously during the loading process. For the outward fronds, large amounts of small fragments could be found due to excessive bent and curled downwards, together with matrix cracks and delamination. The length of fragments varied with the distance from the center line of tubal wall (position of the middle wall wedge as shown in Fig. 8(c)). Shear failure could also be observed in the inward folding. The indicators of crashworthiness, e.g. the mean load and energy absorption, were calculated as summarized in Table 1.

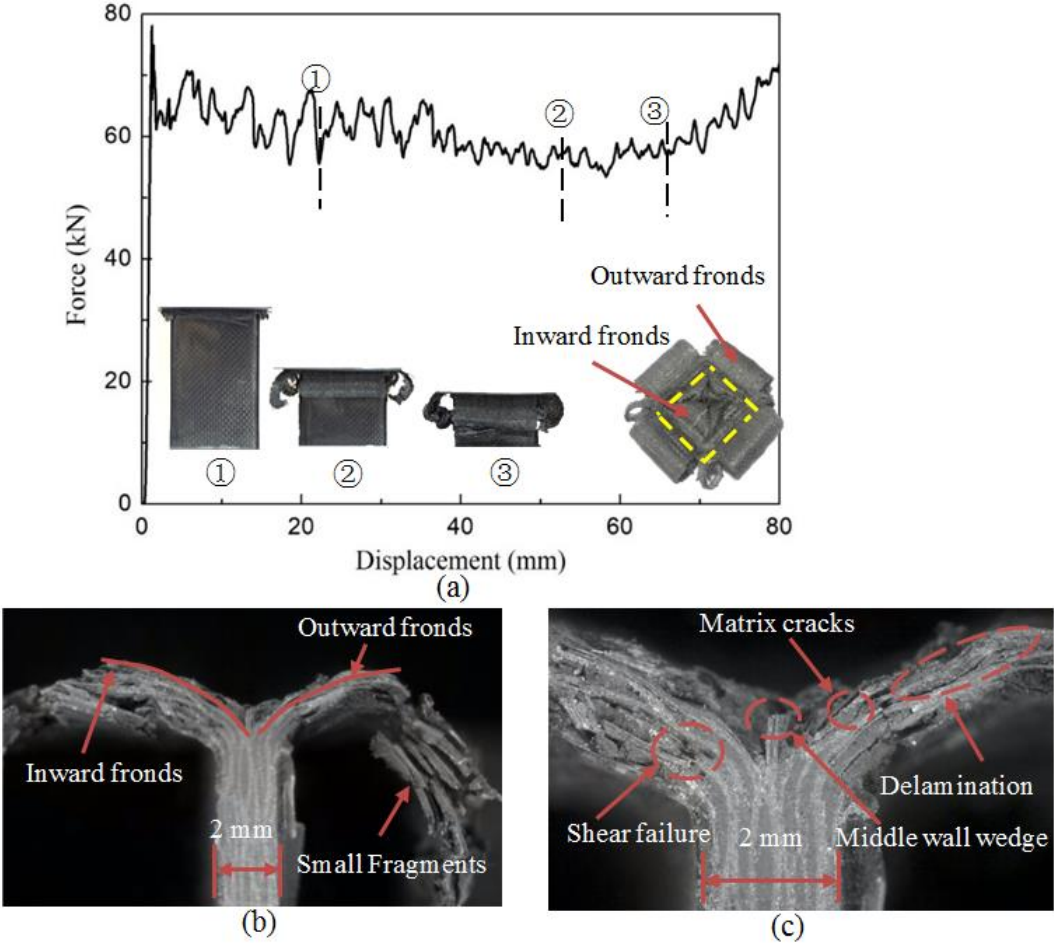


**Fig. 8.** Experimental results of AC: (a) force-displacement curve and damage propagation behavior; (b) and (c) microscopic image after axial crushing.

4.2.2. Specimens with single pre-impact

The axial crushing tests of the singly pre-impacted tube with different energy levels is studied here. Fig. 9 shows the axial force-displacement curves of the CFRP tubes with three pre-impact energies impacted at the same position of P1. There is relatively large difference in comparison with that of non-impacted case (Fig. 8(a)). From Fig. 9, three distinct stages could be identified, namely pre-crushing (stage I), partial loading with local excessive deformation (stage II) and secondary load-bearing (stage III). The corresponding photographs at the four

different crushing stages, specifically  $U = 2 \text{ mm}$ ,  $U = 10 \text{ mm}$ ,  $U = 20 \text{ mm}$  and  $U = 48 \text{ mm}$  (near the pre-impacted penetration area) are shown in Fig. 10 for better understanding of the progressive crushing process in the following analysis.

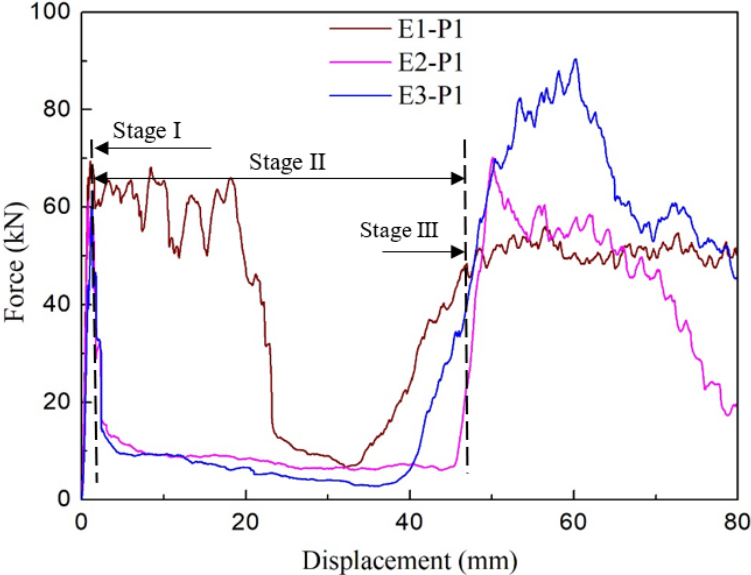


**Fig. 9.** Force-displacement curves after being impacted with different energies.

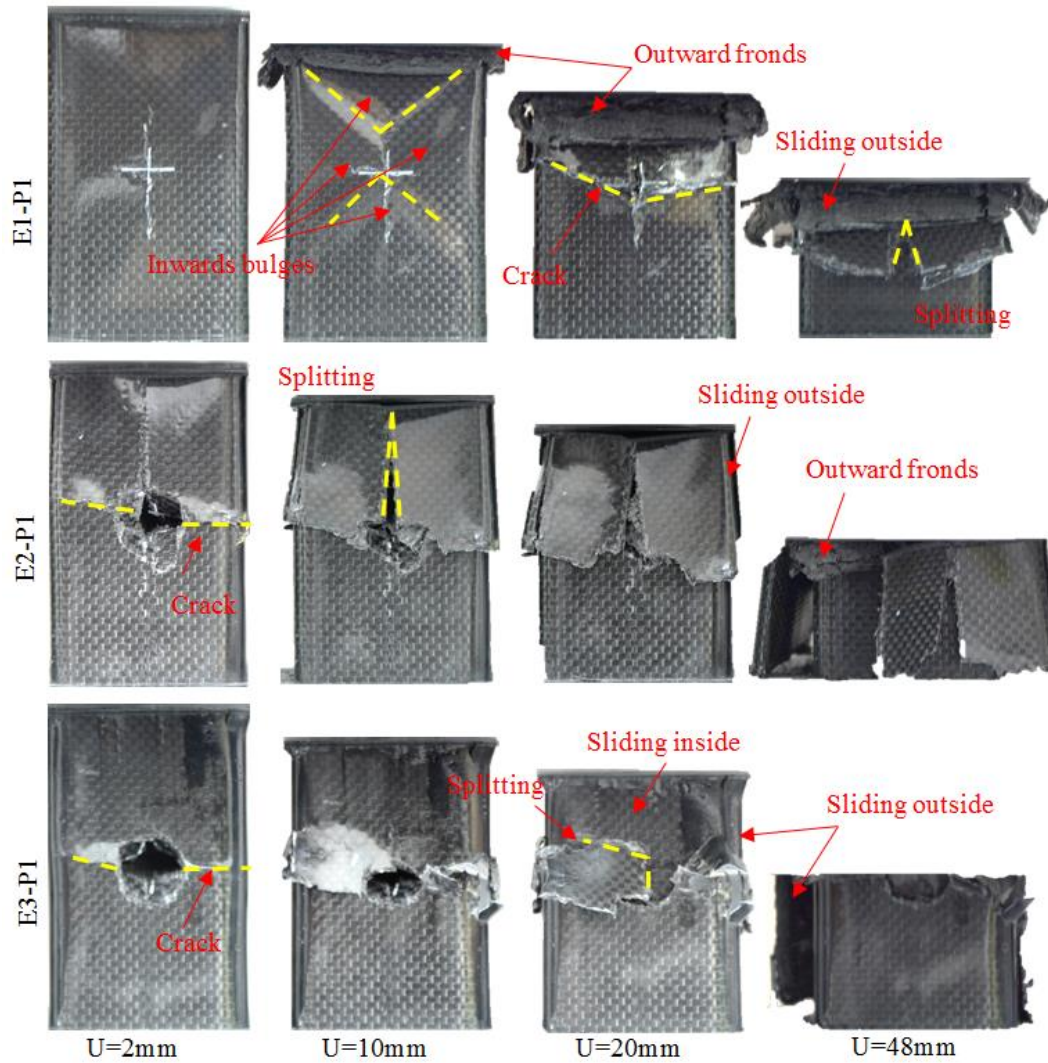


**Fig. 10.** Crushing process of the specimens after being impacted with different energies.

For the singly pre-impacted tube with impact energy of 10 J, the average axial peak crushing force was only 67.8 kN, which is considerably lower than that of the non-impacted specimens (shown in Fig. 8(a)). Different from the failure mode I (as shown in Fig. 8(c)), the loading capacity of CFRP structure appeared partial reduction with progressive failure until the catastrophic drop caused by the transverse pre-impact damage (defined as failure mode II). With increase in the axial crushing displacement up to  $U = 20$  mm, the failure mechanism was mainly from two aspects: a) the accumulation of internal damages near the pre-impact area; and b) cracks propagation in the axial direction (outward fronds as seen in Fig. 10). Several inward bulges on the tubal wall near the pre-impacted damage area were found due to the local stress concentration induced by the pre-impacted damage (Fig. 10). Then the crushing force dropped dramatically to about 10 kN and lasted until the secondary load climbing from the displacement around  $U = 40$  mm. It can be seen from Fig. 10 that cracks appeared around the edges of the pre-impact position and grew circumferentially along the

perimeter of the tubal walls, which led to catastrophic fracture of the upper half tube into several pieces and then slipped toward inside or outside the lower half of the tube. This can be further seen from an isometric view as shown in Fig. 11 ( $U = 48$  mm). In the third stage, the resistant load increased dramatically to 50 kN, which was approximately equal to that prior to  $U = 10$  mm with the progressive folding and delamination of the lower half of the tubal walls. Further validations can be conducted with partial crack fronds, inward and outward fronds as shown in Fig. 12.

The axial force-displacement curves for 20 J and 30 J shared many common features and exhibited a rather different mode with E1-P1 (10 J) which was classified to be failure mode III as summarized in Table 1. The contact force increased rapidly to a peak (at about  $U = 2$  mm) after the loading platen contacted with the incident end of tube (stage I: pre-crushing). Then the load decreased drastically to a relatively stable level around 9 kN (approximately 15% of the peak force). The significant drop of reaction force was due to the cracks initiated near the pre-impacted damage zone and propagated along the circumference of tubal walls as seen from Fig. 10 and Fig. 11. Subsequently, the upper half of the tube split into several pieces until the crushing load climbed again at about  $U = 40$  mm. In this stage, it can be found that little difference between the force-displacement curves existed regardless of the different failure modes and damage evolution processes of the upper half tube (namely, the residual pieces split in the axial direction, sliding inside or outside the lower half of the tube). Finally, the load increased to a new peak as seen in Fig. 9 and then decreased gradually due to the complex fracture mechanism as seen in Fig. 10. Also, a relatively less extent of progressive folding in the upper and lower halves of E2-P1/E3-P1 could be found compared with that of the E1-P1 case.

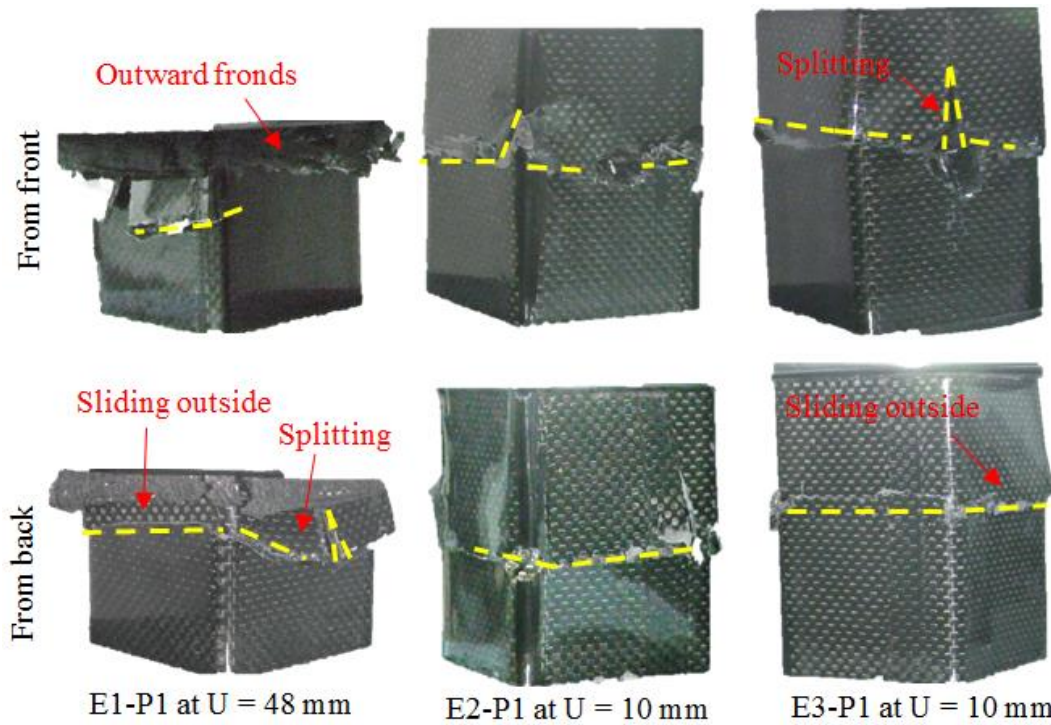


**Fig. 11.** Illustration of the crack initiation and propagation of the specimens during tests in isometric views.

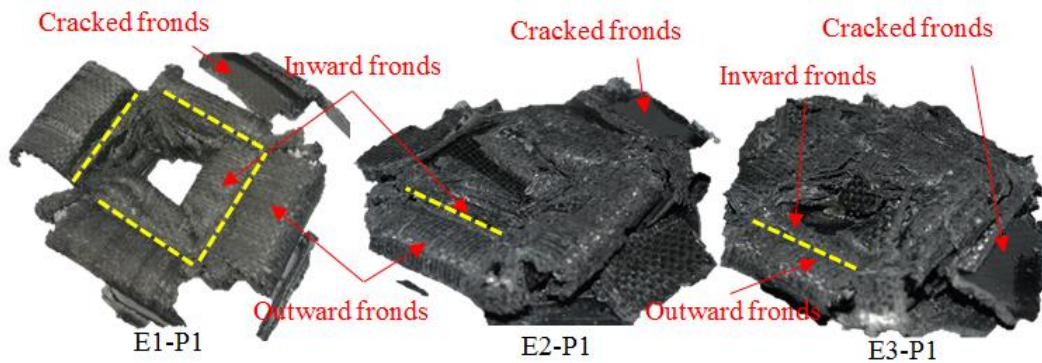


**Fig. 12.** Final crushing failure modes of the pre-impacted specimens with different impact energies.

#### 4.2.3. Specimens with double pre-impacts at different positions

This section investigated the effects of impact position on residual axial crushing performance with the same pre-impact energy and double pre-impacts. Fig. 13 shows the typical force-displacement histories of the pre-damaged specimens with the same number of impacts (2) at the different positions (20 J energy for each impact). Evolution of crushing failure can be observed from an isometric view in Fig. 14. Both the specimens presented similar patterns of force-displacement curves. The crushing load increased rapidly to the first peak after contact, similarly to Section 4.2.2. As crushing deformation proceeded further, circumferential crack and local buckling occurred due to the fracture of tubal walls caused by stress concentration. In the final stage, the progressive folding took place, leading to a relatively stable and high loading process. It can be concluded that the pre-impact positions

dominated the failure process but had only marginal influence on the loading capacity. This can be explained through examining the final failure modes as shown in Fig. 15, where progressive delamination of tubal walls and cracked fronds can be identified, indicating a complex failure mechanism.

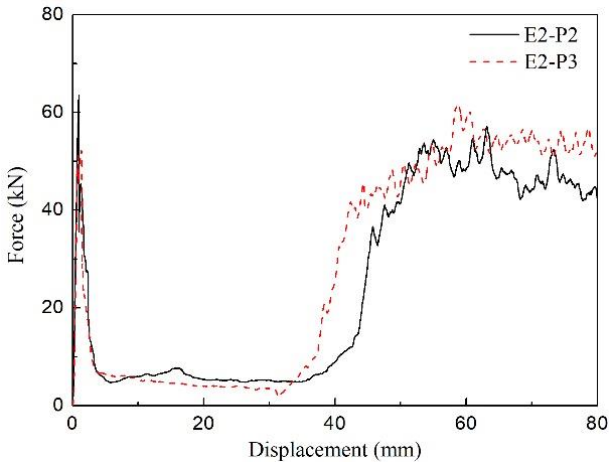


Fig. 13. Force-displacement curves of the specimens with two pre-impacts at different positions.

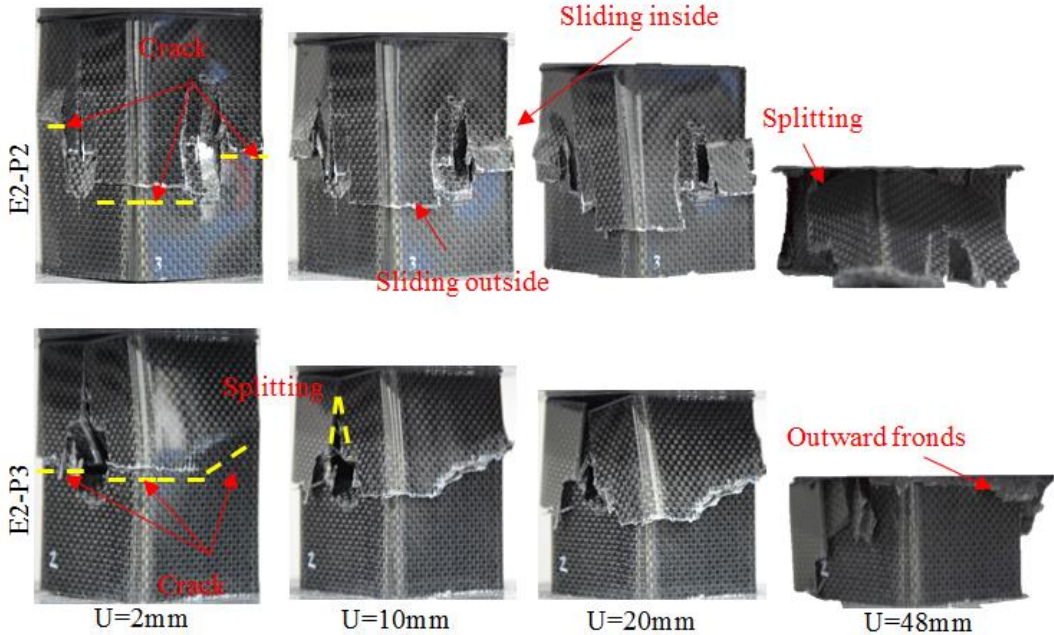
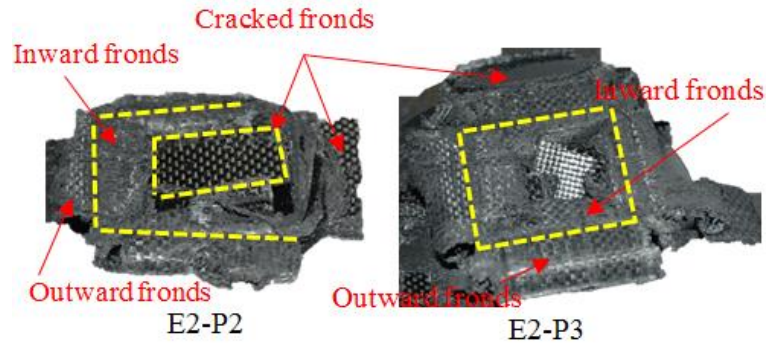


Fig. 14. Crushing process of the specimens with pre-impacts at different positions.



**Fig. 15.** Final crushing failure modes of the specimens with pre-impacts at different positions.

#### 4.2.4. Effects of transverse pre-impacts on axial crushing characteristics

The aforementioned results demonstrated the effects of pre-impact energy/position on residual axial crushing performance. Detailed results, such as peak force, mean load, crush force efficiency and energy absorption, are compared in Table 1. Further assessment is conducted based on the mean values and error bars of all the specimens as shown in Fig. 16.

Reduction about 28% in the peak force (from 83.2 kN to 59 kN) can be observed with the increase of the pre-impact energy from 0 J (non-impact) to 20 J (single pre-impact) in Fig. 16 (a). Nevertheless, when the impact energy increased to 30 J, the peak force remained almost unchanged due to the similar failure mode as depicted in Section 4.1.2. The reason was due to the fact that the failure area of fiber and matrix damage caused by the pre-impact increased from the local indentation damage to complete perforation of the wall; thus, the load bearing capacity reduced mostly. After complete perforation, there was no room for further increase in damage and failure area as shown in Fig. 5, indicating no increase in residual capacity of crushing resistance. This result is also similar to that from the study on the load bearing capacity of perforated square tubes [17], where the holes with different diameters, rather than pre-impacted damage or perforation, were prepared for crushing analysis, leading to a 3-22% reduction in the residual strength.

For the double pre-impacts with E2 (20 J) at different positions on either the adjacent walls (P2) or opposite walls (P3) (refer to Fig. 2), it can be observed from Fig. 16 (a) that the peak impact force at the P3 position (51.5 kN) was about 18% lower than that on P2 position (62.8 kN). On contrary, a relatively small variation in the peak force can be found between the double pre-impacts at the adjacent P2 position and the single pre-impact. This result differs with that from [17], where peak force remained almost unchanged regardless of distribution of the two holes on the adjacent or on the opposite walls. The mean crushing forces of E2-P2 (25 kN) was similar to E2-P1 (24.7 kN) but an approximately 12.9% reduction in comparison with E2-P3 (28.7 kN).

Figs. 16 (c)-(d) show the effect of pre-impacts on the CFE and energy absorption ( $E_a$ ) of axial crushing characteristics. It is interesting to see the same trends of CFE and  $E_a$ . With the increase in the pre-impact energy (from 0J to 20 J), the axial CFE and energy absorption declined 41.6% (from 72% to 42%) and 58.7% (from 48.3J to 19.8J), respectively, indicating significant reduction in the residual capacity of energy absorption in the post-crushing stage. There are significant increases in the CFE and energy absorption from E3-P1 to E2-P1 (similar trends exists between E2-P2 and E2-P3), where the perforation damage state caused by pre-impact loading showed little difference as showed in section 4.1.3. This can be owned to the cracked walls slipped inside the tube in the post-crushing stage, which increased the resistant force as analyzed in Sections 4.2.2-4.2.3.

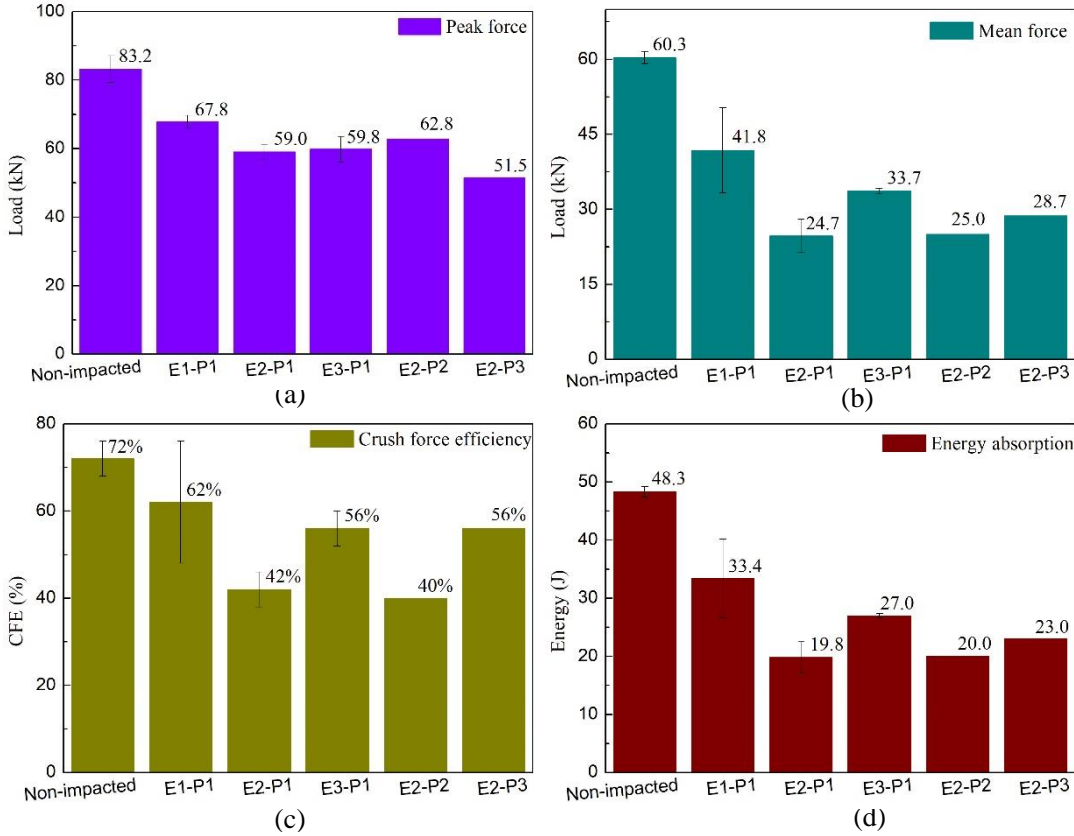
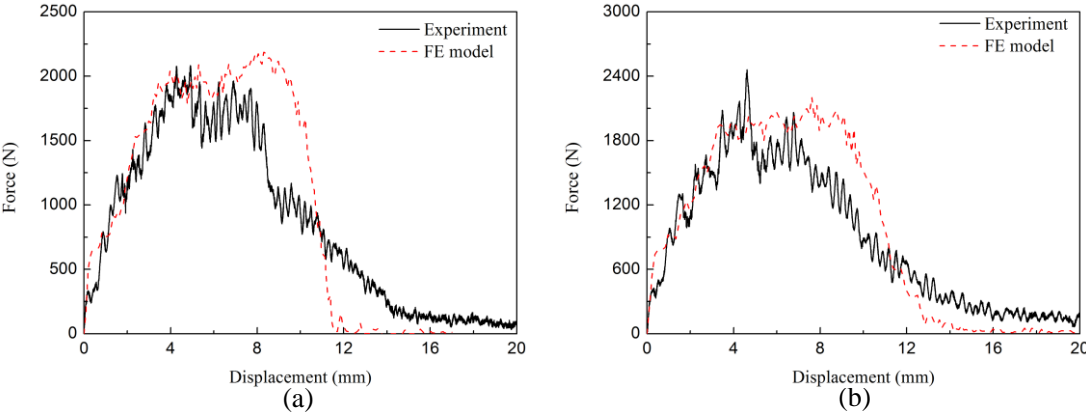


Fig. 16. Effects of pre-impact energy and position on: (a)  $F_{max}$ , (b)  $F_{mean}$  (c)  $CFE$  and (d)  $E_a$ .

### 4.3. Comparison between experimental and numerical modeling

According to Table 1, the impact behaviors showed similar trend under pre-impact energies 20 J and 30 J (complete perforation); and failure III appeared in the most cases for the tubes pre-impacted with energies of 20 J/30 J or at different positions. For this reason, the impactor was assigned the initial dynamic energies of 20 J and 30 J in the numerical models.

As shown in Fig. 17, the force-displacement curves extracted from the FE model agreed with that obtained from the experimental pre-impact tests reasonably well. Computational analyses were only terminated when the pre-impact force dropped to almost zero with complete perforation.



**Fig. 17.** Impact force-displacement curves with energy of: (a) 20 J and (b) 30 J.

*4.3.1. Damage induced during impact*

A comparison of experimental and numerical results of the final failure modes for the tube impacted with 20 J is shown in Fig. 18. The circular perforation through the CFRP wall shows good agreement with the experimental observation. There are four main separated pieces generated near the impact position as seen from both experiment and numerical results.

The primary damage modes, such as fiber fracture, delamination and matrix damage in the walls were discussed in [21]. Fig. 19 shows the distribution of fiber fracture of each CFRP plies and delamination in the interface when fiber failure initiated in the first ply on the impacted site. The variable of CSDMG (corresponds to scalar stiffness degradation for cohesive surfaces) was adopted here to model the damage state for the cohesive interfacial failure. Fiber tensile damage caused by the pre-impact load mainly appeared near the impact position. It can be also observed that the area of fiber tensile damage developed from the outer ply to the inner ply, which agreed well with the final failure mode in the experiment. Delamination contours at each ply-pair interface were concentrated around the impact region. Interfacial failure area in the penetration position decreased from the outer ply to the inner ply, resulting in substantial energy dissipation during the pre-impact process.

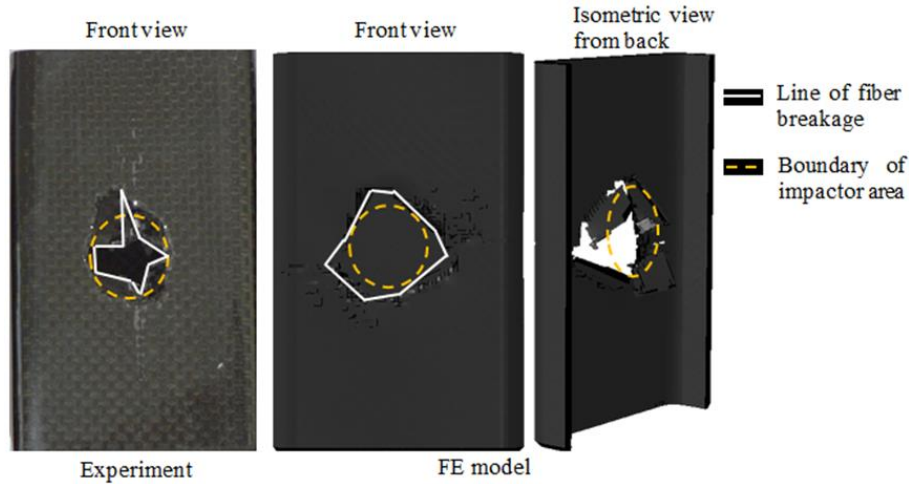


**Fig. 18.** Experimental and numerical results of failure mode for the tube pre-impacted with 20 J.

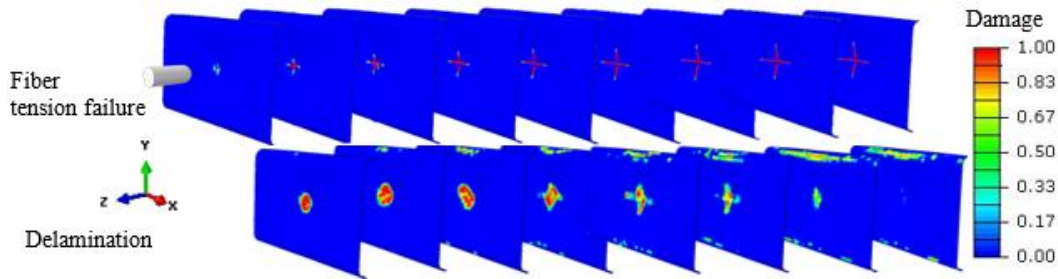


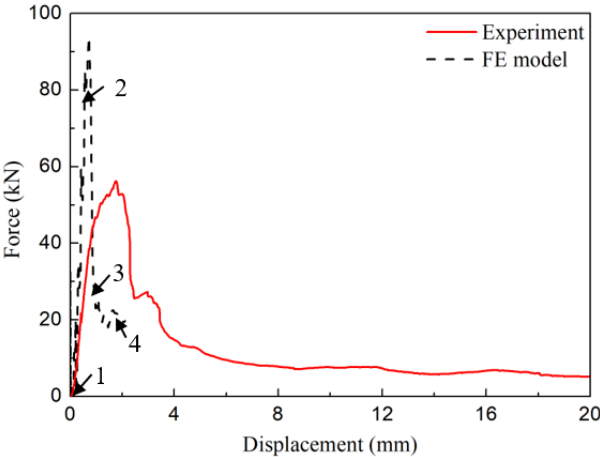
**Fig. 19.** Damage contours on the pre-impacted surface for the tube pre-impacted with 20 J at the time of first ply failure.

#### 4.3.2. Failure in the axial crushing stage

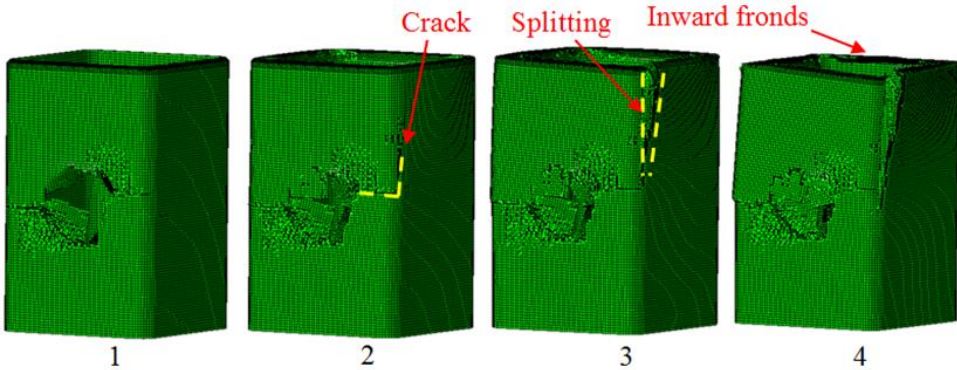
Comparison of axial crushing force-displacement curves for perforated tube (E2-P1) is shown in Fig. 20. It can be observed that, nevertheless, the FE model predicted the trends of crushing force-displacement curves with limited accuracy. This is because the FE modeling accuracy of pre-impacted damage could be carried forward to the subsequent axial crushing stage. As shown in Fig. 17(a), although the FE peak pre-impact load was fairly close to the experimental results, the FE result exhibited a longer plateau of displacement, indicating that removal of the damaged elements was unable to replicate the experimental test accurately. These elements would have continuously borne axial loading in the crushing stage, making the peak load substantially higher. However, these elements were removed under the axial crushing load rather quickly, making the displacement smaller than the experimental crushing test.

Fig. 21 shows the FE prediction of failure mode for the perforated tube with the pre-impact energy of 20 J at different crushing stages as shown in Fig. 20. It is observed that the crack initiated and propagated quickly, thus decreasing loading capacity. Several inwards

bulges appeared on the top end wall near the contact area due to delamination of CFRP plies. Then the brittle unstable cracks initiated and propagated around the perforated hole in the circumferential direction as the crushing load increased, which led to reduction of load bearing capacity of the tube. The cracks around the corners were mainly caused by the shear damage due to stress concentration. The position of the longest initial crack was slightly different with the one observed from the experiment due to the complex failure mechanism. Nevertheless, the FE model predicted the sudden drop of load bearing capacity in the crushing process.



**Fig. 20.** Comparison of crushing force-displacement curves between the experimental and numerical results (pre-impact energy 20J).



**Fig. 21.** Numerical prediction of crack initiation on the pre-impacted tubes.

### 5. Conclusions

In this study, the effects of transverse damage induced by the transverse pre-impact on the axial load bearing capacity and failure behavior of the square CFRP composite tubes have been investigated by using the experimental and finite element modeling approaches. The

CFRP tubes with transversely pre-impacted damage were tested through quasi-static crushing in the axial direction. The failure mechanisms of transverse pre-impact and axial crushing was studied in detail through finite element analysis with a user-defined material model. Within its limitations, the following conclusions can be drawn:

(1) Two different failure modes were observed in the axial quasi-static crushing test for the specimens with single pre-impact. With the increase in the pre-impact energy, the residual crashworthiness performance decreased in terms of peak force, mean force, energy absorption and crush force efficiency.

(2) The residual crushing capacity and the failure mode were more dependent on the pre-impact energy than impact position. Compared with single pre-impact (e.g. E2-P1 with impact energy of 20J), the specimen with adjacent double pre-impacting positions (P2) showed slight reduction in the residual crushing energy absorption capacity while the opposite position had a marginal increase of 16.2% (P3).

(3) FE simulation showed that the CDM (continuum damage mechanics) model was able to properly replicate the different failure modes such as fiber failure and delamination caused by the pre-impact damage in the first stage. In the second stage, the FE model allows to predict the axial crushing behavior in terms of crack initiation and propagation. However, further study is still needed to enhance the accuracy of such a two-stage crushing process.

(4) Besides the residual crashworthiness of CFRP structures with pre-impact damage under axial crushing, the residual performance of CFRP structures with pre-impact damage under oblique [34-37] and transverse loading [38, 39] also should be comprehensively investigated in the future.

## **Acknowledgments**

This work is supported by National Natural Science Foundation of China (51575172, 51475155) and the Open Fund of the State Key Laboratory for Strength and Vibration of Mechanical Structures of Xi'an Jiaotong University (SV2017-KF-24). Dr Guangyong Sun is a recipient of Australian Research Council (ARC) Discovery Early Career Researcher Award (DECRA) in the University of Sydney.

## **References**

[1] P. Feraboli, A. Masini, L. Taraborrelli, A. Pivetti, Integrated development of CFRP structures for a topless high performance vehicle, *Composite Structures* 78(4) (2007) 495-506.

- [2] Q. Liu, Y. Lin, Z. Zong, G. Sun, Q. Li, Lightweight design of carbon twill weave fabric composite body structure for electric vehicle, *Composite Structures* 97 (2013) 231-238.
- [3] J. Obradovic, S. Boria, G. Belingardi, Lightweight design and crash analysis of composite frontal impact energy absorbing structures, *Composite Structures* 94(2) (2012) 423-430.
- [4] G. Sun, H. Zhang, J. Fang, G. Li, Q. Li, Multi-objective and multi-case reliability-based design optimization for tailor rolled blank (TRB) structures, *Structural and Multidisciplinary Optimization* 55(5) (2017) 1899-1916.
- [5] Q. Liu, Z. Ou, Z. Mo, Q. Li, D. Qu, Experimental investigation into dynamic axial impact responses of double hat shaped CFRP tubes, *Composites Part B: Engineering* 79 (2015) 494-504.
- [6] A.G. Mamalis, D.E. Manolakos, M.B. Ioannidis, D.P. Papapostolou, On the response of thin-walled CFRP composite tubular components subjected to static and dynamic axial compressive loading: experimental, *Composite Structures* 69(4) (2005) 407-420.
- [7] A.G. Mamalis, D.E. Manolakos, M.B. Ioannidis, D.P. Papapostolou, Crashworthy characteristics of axially statically compressed thin-walled square CFRP composite tubes: experimental, *Composite Structures* 63(3-4) (2004) 347-360.
- [8] X. Jia, G. Chen, Y. Yu, G. Li, J. Zhu, X. Luo, C. Duan, X. Yang, D. Hui, Effect of geometric factor, winding angle and pre-crack angle on quasi-static crushing behavior of filament wound CFRP cylinder, *Composites Part B: Engineering* 45(1) (2013) 1336-1343.
- [9] D. Siromani, G. Henderson, D. Mikita, K. Mirarchi, R. Park, J. Smolko, J. Awerbuch, T.-M. Tan, An experimental study on the effect of failure trigger mechanisms on the energy absorption capability of CFRP tubes under axial compression, *Composites Part A: Applied Science and Manufacturing* 64 (2014) 25-35.
- [10] J. Meredith, E. Bilson, R. Powe, E. Collings, K. Kirwan, A performance versus cost analysis of prepreg carbon fibre epoxy energy absorption structures, *Composite Structures* 124 (2015) 206-213.
- [11] C. McGregor, R. Vaziri, X. Xiao, Finite element modelling of the progressive crushing of braided composite tubes under axial impact, *International Journal of Impact Engineering* 37(6) (2010) 662-672.
- [12] G. Zhu, G. Sun, G. Li, A. Cheng, Q. Li, Modeling for CFRP structures subjected to quasi-static crushing, *Composite Structures* 184 (2018) 41-55.
- [13] X. Xiao, M.E. Botkin, N.L. Johnson, Axial crush simulation of braided carbon tubes using MAT58 in LS-DYNA, *Thin-Walled Structures* 47(6-7) (2009) 740-749.
- [14] D. Siromani, J. Awerbuch, T.-M. Tan, Finite element modeling of the crushing behavior of thin-walled CFRP tubes under axial compression, *Composites Part B: Engineering* 64 (2014) 50-58.
- [15] B.P. Bussadori, K. Schuffenhauer, A. Scattina, Modelling of CFRP crushing structures in explicit crash analysis, *Composites Part B: Engineering* 60 (2014) 725-735.
- [16] Q. Liu, O. Guo, Y. Ju, Y. Lin, Q. Li, Impact responses and residual flexural properties of narrow CFRP laminates, *Composite Structures* 111 (2014) 332-339.
- [17] Q. Liu, J. Ma, X. Xu, Y. Wu, Q. Li, Load bearing and failure characteristics of perforated square CFRP tubes under axial crushing, *Composite Structures* 160 (2017) 23-35.
- [18] E. Guades, T. Aravinthan, Residual properties of square FRP composite tubes subjected to repeated axial impact, *Composite Structures* 95 (2013) 354-365.
- [19] T.A. Sebaey, E. Mahdi, Crashworthiness of pre-impacted glass/epoxy composite tubes, *International Journal of Impact Engineering* 92 (2016) 18-25.
- [20] S.X. Wang, L.Z. Wu, L. Ma, Low-velocity impact and residual tensile strength analysis to carbon fiber composite laminates, *Materials & Design* 31(1) (2010) 118-125.
- [21] M.R. Abir, T.E. Tay, M. Ridha, H.P. Lee, Modelling damage growth in composites subjected to impact and compression after impact, *Composite Structures* 168 (2017) 13-25.
- [22] W. Tan, B.G. Falzon, L.N.S. Chiu, M. Price, Predicting low velocity impact damage and Compression-After-Impact (CAI) behaviour of composite laminates, *Composites Part A: Applied Science and Manufacturing* 71 (2015) 212-226.
- [23] E.V. González, P. Maimí, P.P. Camanho, A. Turon, J.A. Mayugo, Simulation of drop-weight impact and compression after impact tests on composite laminates, *Composite Structures* 94(11) (2012) 3364-3378.
- [24] S. Rivallant, C. Bouvet, N. Hongkarnjanakul, Failure analysis of CFRP laminates subjected to compression after impact: FE simulation using discrete interface elements, *Composites Part A: Applied Science and Manufacturing* 55 (2013) 83-93.
- [25] P.A.A.E. Mendes, M.V. Donadon, Numerical prediction of compression after impact behavior of woven composite laminates, *Composite Structures* 113 (2014) 476-491.
- [26] G. Zhu, G. Sun, Q. Liu, G. Li, Q. Li, On crushing characteristics of different configurations of metal-composites hybrid tubes, *Composite Structures* 175 (2017) 58-69.
- [27] M.E. Deniz, R. Karakuzu, M. Sari, B.M. Icten, On the residual compressive strength of the glass-epoxy tubes

- subjected to transverse impact loading, *Journal of Composite Materials* 46(6) (2011) 737-745.
- [28] G. Sun, S. Li, Q. Liu, G. Li, Q. Li, Experimental study on crashworthiness of empty/aluminum foam/honeycomb-filled CFRP tubes, *Composite Structures* 152 (2016) 969-993.
- [29] M.V. Donadon, L. Iannucci, B.G. Falzon, J.M. Hodgkinson, S.F.M. de Almeida, A progressive failure model for composite laminates subjected to low velocity impact damage, *Computers & Structures* 86(11-12) (2008) 1232-1252.
- [30] V.S. Sokolinsky, K.C. Indermuehle, J.A. Hurtado, Numerical simulation of the crushing process of a corrugated composite plate, *Composites Part A: Applied Science and Manufacturing* 42(9) (2011) 1119-1126.
- [31] Y. Shi, T. Swait, C. Soutis, Modelling damage evolution in composite laminates subjected to low velocity impact, *Composite Structures* 94(9) (2012) 2902-2913.
- [32] Hibbitt, Karlsson, Sorensen, ABAQUS/standard User's Manual, Hibbitt, Karlsson & Sorensen 2001.
- [33] D. Liu, Characterization of Impact Properties and Damage Process of Glass/Epoxy Composite Laminates, *Journal of Composite Materials* 38(16) (2004) 1425-1442.
- [34] G. Sun, T. Liu, J. Fang, G.P. Steven, Q. Li, Configuration optimization of multi-cell topologies for multiple oblique loads, *Structural and Multidisciplinary Optimization* 57(2) (2018) 469-488.
- [35] G. Zhu, G. Sun, H. Yu, S. Li, Q. Li, Energy absorption of metal composite and metal/composite hybrid structures under oblique crushing loading, *International Journal of Mechanical Sciences* 135 (2018) 458-483.
- [36] G. Sun, S. Li, G. Li, Q. Li, On crushing behaviors of aluminium/CFRP tubes subjected to axial and oblique loading: An experimental study, *Composites Part B: Engineering* 145 (2018) 47-56.
- [37] G. Li, F. Xu, G. Sun, Q. Li, A comparative study on thin-walled structures with functionally graded thickness (FGT) and tapered tube withstanding oblique impact loading, *International Journal of Impact Engineering* 77 (2015) 68-83.
- [38] H. Zhang, G. Sun, Z. Xiao, G. Li, Q. Li, Bending characteristics of top-hat structures through tailor rolled blank (TRB) process, *Thin-Walled Structures* 123 (2018) 420-440.
- [39] G. Sun, T. Pang, G. Zheng, J. Song, Q. Li, On energy absorption of functionary graded tubes under transverser loading, *International Journal of Mechanical Sciences* 115 (2016) 465-480.